

A 10 kpc SCALE SEYFERT GALAXY OUTFLOW: *HST*/COS OBSERVATIONS OF IRAS F22456–5125

BENOIT C. J. BORGUET¹, DOUG EDMONDS¹, NAHUM ARAV¹, JAY DUNN², AND GERARD A. KRISS^{3,4}

¹ Department of Physics, Virginia Tech, Blacksburg, VA 24061, USA; benbo@vt.edu

² Augusta Perimeter College, Atlanta, GA, USA

³ Space Telescope Science Institute, 3700 San Martin Drive, Baltimore, MD 21218, USA

⁴ Center for Astrophysical Sciences, Department of Physics and Astronomy, Johns Hopkins University, Baltimore, MD 21218, USA

Received 2012 January 6; accepted 2012 March 25; published 2012 May 11

ABSTRACT

We present analysis of the UV spectrum of the low- z AGN IRAS F22456–5125 obtained with the Cosmic Origins Spectrograph on board the *Hubble Space Telescope*. The spectrum reveals six main kinematic components, spanning a range of velocities of up to 800 km s^{-1} , which for the first time are observed in troughs associated with C II, C IV, N V, Si II, Si III, Si IV, and S IV. We also obtain data on the O VI troughs, which we compare to those available from an earlier *Far Ultraviolet Spectroscopic Explorer* epoch. Column densities measured from these ions allow us to derive a well-constrained photoionization solution for each outflow component. Two of these kinematic components show troughs associated with transitions from excited states of Si II and C II. The number density inferred from these troughs, in combination with the deduced ionization parameter, allows us to determine the distance to these outflow components from the central source. We find these components to be at a distance of $\sim 10 \text{ kpc}$. The distances and the number densities derived are consistent with the outflow being part of a galactic wind.

Key words: galaxies: active – line: formation – quasars: absorption lines – quasars: individual (IRAS F22456–5125)

Online-only material: color figures, figure set

1. INTRODUCTION

Mass outflows are detected in the UV spectra of more than 50% of low-redshift active galactic nuclei (AGNs), mainly Seyfert galaxies, e.g., Crenshaw et al. (1999), Kriss et al. (2002), Dunn et al. (2007), and Ganguly & Brotherton (2008). These outflows are observed as narrow absorption lines (a few hundred km s^{-1} in width) blueshifted with respect to the AGN systemic redshift.

In this paper, we determine the ionization equilibrium, distance, mass flow rate, and kinetic luminosity of the UV outflow observed in the luminous Seyfert 1 galaxy IRAS F22456–5125 ($z = 0.1016$; Dunn et al. 2010). The bolometric luminosity of this object, $L_{\text{bol}} = 10^{45.6} \text{ erg s}^{-1}$ (see Section 4), places it at the Seyfert/quasar border defined to be $10^{12} L_{\odot}$, where L_{\odot} is the luminosity of the Sun (Soifer et al. 1987). Several absorption systems are resolved in the UV spectrum in five main kinematic components ranging in velocity from -20 km s^{-1} to -820 km s^{-1} . A detailed analysis of the physical properties of the UV absorber determined from *Far Ultraviolet Spectroscopic Explorer* (*FUSE*) archival spectra has been published by Dunn et al. (2010). These authors report a lower limit on the distance R of the absorbing material from the central source of 20 kpc using photoionization timescale arguments.

In 2010 June we observed IRAS F22456–5125 with the Cosmic Origins Spectrograph (COS) on board the *Hubble Space Telescope* (*HST*) as part of our program aiming at determining the cosmological impact of AGN outflows (PI: Arav, PID: 11686). The high signal-to-noise spectrum obtained reveals the presence of absorption troughs associated with high-ionization species (C IV, N V, O VI, Si IV, and S IV), as well as lower ones (Si II, Si III, C II), thus increasing the number of constraints on the photoionization analysis of the absorber compared to Dunn et al. (2010). We also identify absorption troughs

corresponding to excited states of Si II and C II associated with two kinematic components of the UV outflow. The population of the excited state relative to the resonance counterpart provides an indirect measurement of the number density of the gas producing the lines (Osterbrock & Ferland 2006). These number densities allow us to determine reliable distances to these two components and hence derive their mass flow rates and kinetic luminosities.

The plan of the paper is as follows: in Section 2, we present the COS observations of IRAS F22456–5125, as well as the reduction of the data and identification of the spectral features within the COS range. In Section 3, we detail the computation of the column densities associated with every species. We present the photoionization analysis of the outflow components in Section 4 and report the derived distance, mass flow rate, and kinetic luminosity in Section 5. We conclude the paper by a discussion of our results in Section 6. This paper is the second of a series and the reader will be referred to Edmonds et al. (2011, hereafter Paper I) for further details on the techniques used throughout the paper.

2. *HST*/COS OBSERVATIONS AND DATA REDUCTION

We observed IRAS F22456–5125 using the COS instrument (Osterman et al. 2011) on board the *HST* in 2010 June using both medium-resolution ($\Delta\lambda/\lambda \sim 18,000$) far ultraviolet gratings G130M and G160M. Sub-exposures of the target were obtained for each grating through the Primary Science Aperture using different central wavelength settings in order to minimize the impact of the instrumental features and to fill the gap between detector segments, providing a continuous coverage over the spectral range between roughly $1135\text{--}1795 \text{ \AA}$. We obtained a total integration time of $15,056 \text{ s}$ and $11,889 \text{ s}$ for the G130M and G160M gratings, respectively.

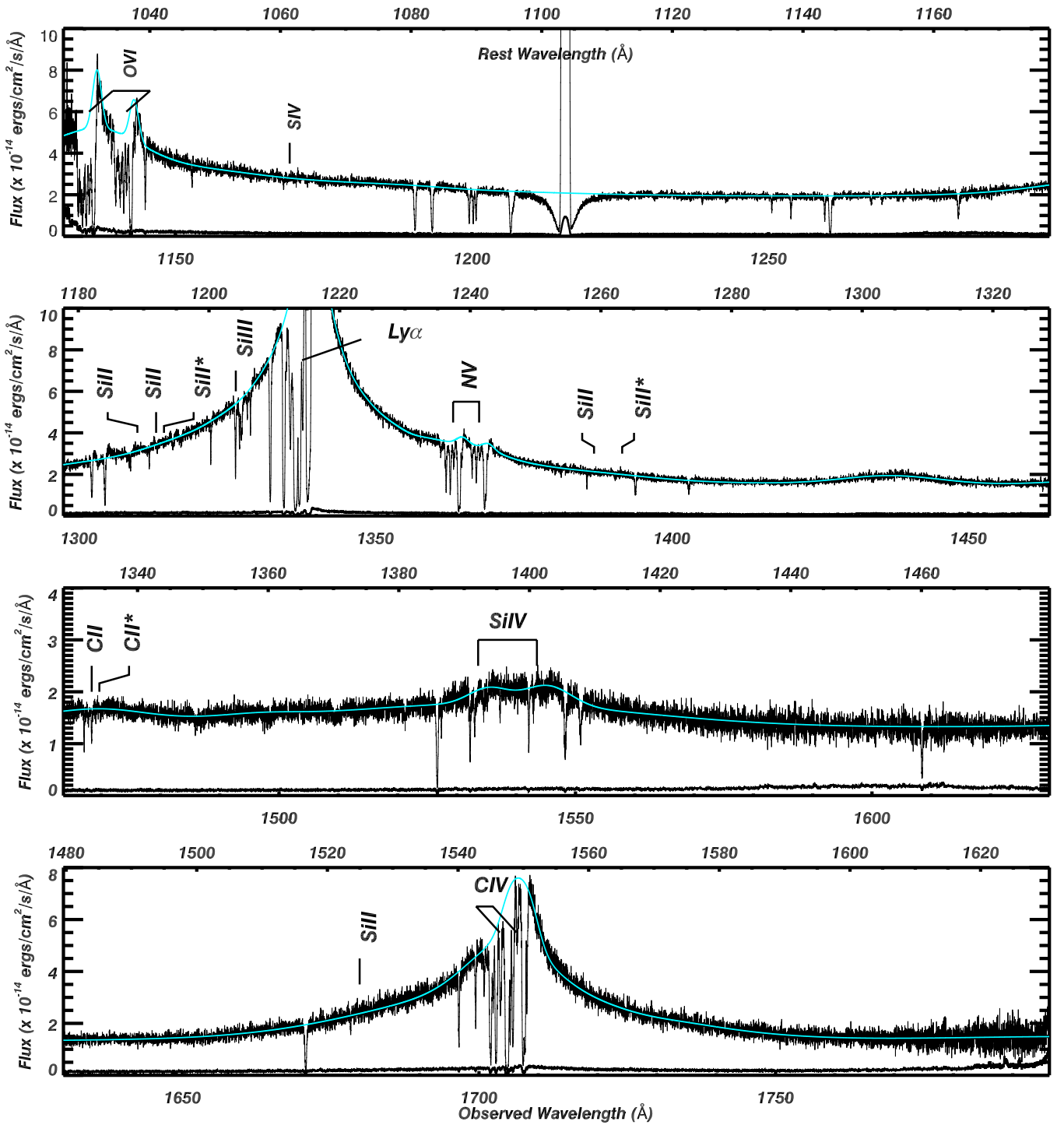


Figure 1. Full FUV spectrum of IRAS F22456–5125 obtained by COS. The major absorption troughs related to the intrinsic absorber are labeled. The green line represents our fit to the non-absorbed emission model (see Section 2.3).

(A color version and the complete figure set (23 images) of this figure are available in the online journal.)

The data sets processed through the standard CALCOS⁵ pipeline were retrieved from the MAST archive. They were then flat-fielded and combined together using the COADD_X1D⁶ IDL pipeline developed by the COS GTO team (see Danforth et al. 2010 for details). The reduced spectrum with its original

$\sim 2 \text{ km s}^{-1}$ oversampling has an overall signal-to-noise ratio (S/N) $\geq 15 \text{ pixel}^{-1}$ in most of the continuum region. Typical errors in the wavelength calibration are less than 15 km s^{-1} . In Figure 1, we show the majority of the spectrum on which we identified major intrinsic absorption features associated with the outflow. The COS FUV spectrum of IRAS F22456–5125 is presented in greater detail along with the identification of most absorption features (interstellar, intergalactic, and intrinsic lines) in the online version of Figure 1.

⁵ Details on CALCOS can be found in the COS Data Handbook.

⁶ The routine can be found at <http://casa.colorado.edu/~danforth/science/cos/costools.html>.

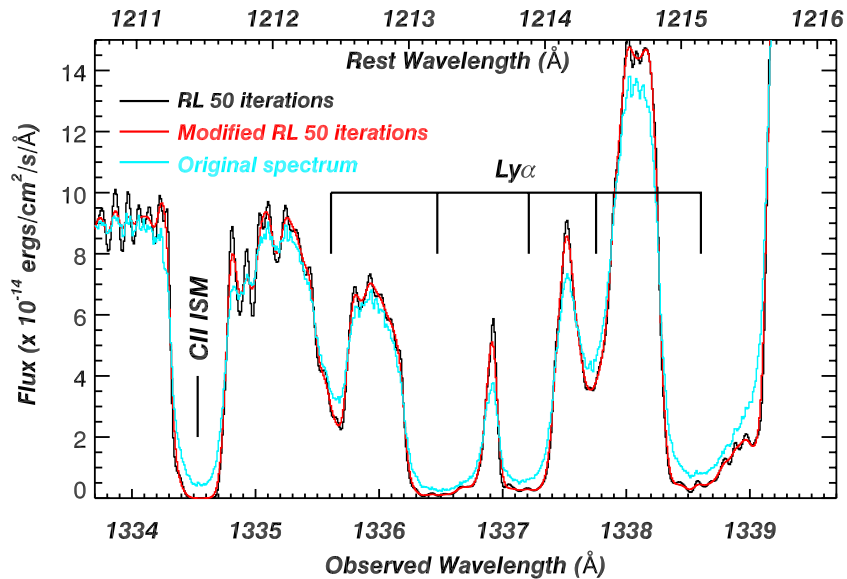


Figure 2. Illustration of the necessity of using a deconvolution algorithm when dealing with COS data (see the text for details). Troughs associated with the intrinsic absorber significantly deepen while the saturated interstellar C II line exhibits the expected squared black bottom profile. The main difference between the deconvolved spectrum using the RL method and the modified RL algorithm respecting the sampling theorem is the significant reduction of oscillations due to the total deconvolution process performed in RL, even more so when considering a high number of iterations.

(A color version of this figure is available in the online journal.)

2.1. Identification of Spectral Features

Using archived *FUSE* spectra, Dunn et al. (2007, 2010) reported the first detection of five distinct kinematic components with centroid velocities $v_1 = -800$ km s $^{-1}$, $v_2 = -610$ km s $^{-1}$, $v_3 = -440$ km s $^{-1}$, $v_4 = -320$ km s $^{-1}$, $v_5 = -130$ km s $^{-1}$ and FWHM $\in [50, 200]$ km s $^{-1}$ associated with an intrinsic UV outflow in IRAS F22456–5125. These components, spanning a total velocity range of 800 km s $^{-1}$, were detected in O VI, C III, and several lines of the Lyman series (Ly β to Ly η). Using the kinematic pattern reported by Dunn et al. (2010) as a template, we identify absorption features in our COS spectrum related to both low-ionization (C II, Si II, Si III) and high-ionization species (Si IV, S IV, C IV, N V, O VI), as well as in the Ly α transition. Absorption troughs from the metastable level C II* λ 1335.704 are detected in components 2 and 3, and troughs from metastable Si II* λ 1264.738 and 1194.500 are detected in component 2.

While the absorption troughs associated with the higher-ionization lines generally exhibit broader profiles, we observe a 1:1 kinematic correspondence between the core of these components and the narrower features associated with the lower-ionization species of the outflow. Given the significantly broad range of velocities covered by the components and their net kinematic separations, such a match is not likely to occur by chance. This argues in favor of a scenario where the troughs of the different ionic species detected in a given kinematic component are generated in the same region. This observation is strengthened by the fact that most of the troughs have a line profile similar to that of the non-blended N V λ 1238.820 line when properly scaled.

The high S/N of our COS observations (S/N $\gtrsim 40$ per resolution element on most of the spectral coverage) reveals the presence of kinematic substructures in several components of the outflow compared to the lower-S/N *FUSE* observations (S/N ~ 7 ; Dunn et al. 2010). Nevertheless, given the self-blending of these features in the strongest lines (e.g., O VI) and the absence of apparent change between the *FUSE* and COS observations, we will use the labeling of components as defined

in Dunn et al. (2010). We will, however, separate their trough 5 into low- and high-velocity components given the apparent difference in ionization suggested by the presence of a stronger Si III in subcomponent 5A ($v_{5A} = -40$ km s $^{-1}$) than in 5B ($v_{5B} = -130$ km s $^{-1}$) relative to the higher-ionization lines (C IV, N V, O VI; see Figure 3). Most of our analysis in this paper concentrates on components 2 and 3 of the outflow, for which absorption features associated with an excited state have been detected.

2.2. Deconvolution of the COS Spectrum

Detailed analysis of the on-orbit COS line-spread function (LSF) revealed the presence of broadened wings that scatter a significant part of the continuum flux inside the absorption troughs (see Kriss et al. 2011 for details). This continuum leaking is particularly strong for narrow absorption troughs (FWHM ~ 50 km s $^{-1}$) in which this effect may significantly affect the estimation of the true column density by artificially increasing the residual intensity observed inside the troughs.

Given the overall good S/N of our data, we can correct the effect of the poor LSF by deconvolving the COS spectrum. Adopting the procedure described in Kriss et al. (2011), we deconvolve the spectrum obtained for each grating in 50 Å intervals using the wavelength-dependent LSFs and an IDL implementation of the stsdas Richardson–Lucy (RL) “lucy” algorithm (G. Schneider & B. Stobie 2011, private communication). The main effect of the deconvolution is illustrated in Figure 2, in which we clearly see that the deconvolved spectrum shows significantly deepened intrinsic Ly α absorption troughs and produces a square, black bottom for the saturated interstellar line C II λ 1334.532.

However, the main drawback of the deconvolution algorithms commonly used, such as the RL algorithm, is a significant increase of the noise in the deconvolved spectrum due to the fact that these techniques try to perform a total deconvolution of the data, i.e., in which the LSF of the deconvolved spectrum is a Dirac delta function, violating the Shannon sampling theorem

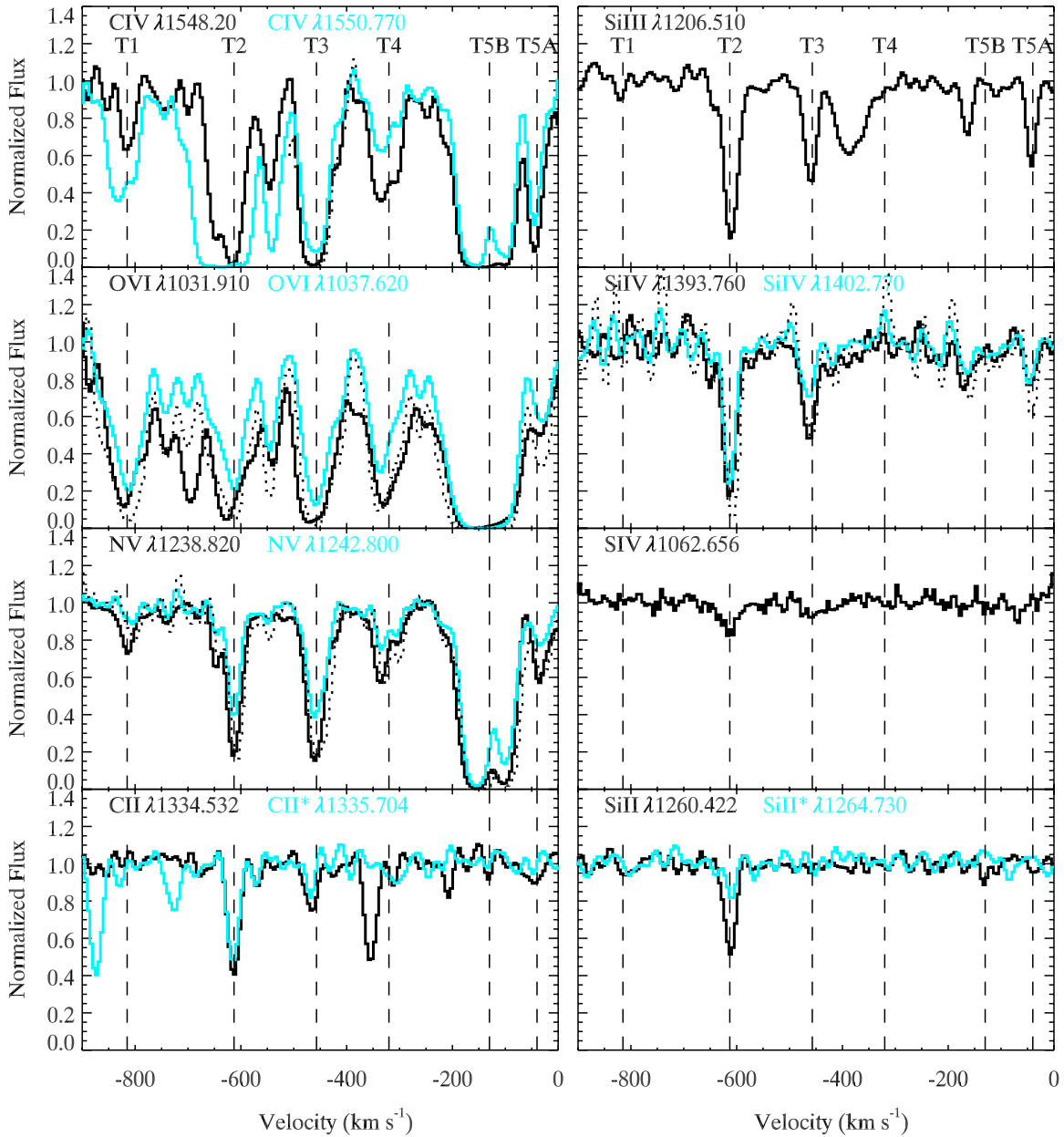


Figure 3. Normalized absorption line profile of the metal lines associated with the outflow in IRAS F22456–5125. The line profiles have been deconvolved using the modified RL algorithm described in Section 2.2 and rebinned to a common $\sim 5 \text{ km s}^{-1}$ dispersion velocity scale. For doublets, we overplot the expected residual intensity in the strongest component based on the residual flux observed in the weakest component assuming an AOD absorber model. For CIV we only plot that quantity in regions free of self-blending (mainly T3; see the text).

(A color version of this figure is available in the online journal.)

(see Magain et al. 1998 for a thorough discussion of these issues). In order to decrease these effects, we modified the RL algorithm by forcing the deconvolved spectrum to have an LSF satisfying the sampling theorem. We choose the deconvolved LSF to be a Gaussian with a 2 pixel FWHM ($\sim 5 \text{ km s}^{-1}$ given the COS detector sampling). This operation prevents the appearance of strong unwanted oscillations since we force the maximum resolution that can be achieved in the deconvolved data to agree with the sampling theorem. The deconvolved spectrum produced by this modified RL algorithm is similar to the one obtained by the traditional RL algorithm (see Figure 2), the main difference being the significant decrease of the high frequencies and high-amplitude features artificially generated by RL deconvolution with a high number of iterations. In our analysis, we will derive the column density for each ionic

species using the spectrum deconvolved with the modified RL algorithm, allowing us to derive more accurate column densities associated with the narrow absorption components observed in IRAS F22456–5125.

2.3. Unabsorbed Emission Model

The unabsorbed emission model $F_0(\lambda)$ of IRAS F22456–5125 is constructed in a similar manner to the one described in detail for IRAS F04250–5718 in Paper I, in which we consider three main sources of emission: a continuum, a broad emission line (BEL) component, and a narrow emission line (NEL) component. Adopting a single power law (PL) $F(\lambda) = F_{1150}(\lambda/1150)^\alpha$ to describe the dereddened ($E(B - V) = 0.01035$; Schlegel et al. 1998) continuum emission, we obtain

a reduced $\chi_{\text{red}}^2 = 1.413$ over emission/absorption line free regions of the rest wavelength spectrum ([1115, 1130] Å, [1340, 1360] Å, and [1455, 1475] Å) with $\alpha = -1.473 \pm 0.068$ and $F_{1150} = 2.13010^{-14} \pm 0.003310^{-14}$ erg cm⁻² Å⁻¹ s⁻¹.

Prominent BEL features observed in the spectrum (Ly α , C IV, O VI) are fit using two broad Gaussians of FWHM ~ 9000 and 2000 km s⁻¹. The NEL component of each line of a doublet is fit by a single narrower Gaussian (FWHM ~ 600 km s⁻¹) centered around the rest wavelength of each line, with the separation of the two Gaussians fixed to the velocity difference between the doublet lines. The NEL of the strong Ly α line is best fit by two Gaussians of FWHM ~ 1200 and 400 km s⁻¹. The remaining weaker emission features in the spectrum (Si IV+O IV, C II, N V, O I, etc.) are modeled by a smooth cubic spline fit. A normalized spectrum is then obtained by dividing the data with the emission model. We present our best fit to the unabsorbed spectrum of IRAS F22456–5125 in Figure 1.

3. COLUMN DENSITY DETERMINATION

3.1. Methodology

The column density associated with a given ionic species detected in the outflow is determined by modeling the residual intensity in the normalized data of the absorption troughs. Assuming a single homogeneous emission source $F_0(v)$ and a one-dimensional spatial distribution of optical depth across the emission source $\tau_i(x, v)$, we can express the intensity $F_i(v)$ observed for a line i as (Arav et al. 2005)

$$F_i(v) = F_0(v) \int_0^1 e^{-\tau_i(x,v)} dx, \quad (1)$$

where v is the radial velocity of the outflow and the spatial extension of the emission source is normalized to 1. Once the optical depth solution $\tau_i(x, v)$ is derived at a given radial velocity, we link the observed residual intensity $I_i(v) = F_i(v)/F_0(v)$ to the ionic column density using the relation

$$N_{\text{ion}}(v) = \frac{3.8 \times 10^{14}}{f_i \lambda_i} \langle \tau_i(v) \rangle (\text{cm}^{-2} \text{ km}^{-1} \text{ s}), \quad (2)$$

where f_i , λ_i , and $\langle \tau_i(v) \rangle$ are the oscillator strength, the rest wavelength, and the average optical depth across the emission source of line i (see Paper I), respectively.

We consider here the three absorber models (i.e., optical depth distributions) discussed in Paper I: the apparent optical depth (AOD), partial covering (PC), and PL models. We use these three models in order to account for possible inhomogeneities in the absorber (see Section 6), which cause the apparent strength ratio $R_a = \tau_i/\tau_j$ of two lines i, j from a given ion to deviate from the expected laboratory ratio $R_l = \lambda_i f_i/\lambda_j f_j$ (e.g., Wampler et al. 1995; Hamann 1997; Arav et al. 1999). Wherever possible we derive these three optical depth solutions for ions with multiple transitions. However, as mentioned in Paper I, we consider the results obtained with the PL model performed on doublets with caution given its increased sensitivity to the S/N, which can lead to severe overestimation of the underlying column density (Arav et al. 2005). For singlet lines we will generally only derive a lower limit on the column density using the AOD method. This lower limit will be considered a measurement in cases where the singlet line is associated with a kinematic component for which other multiplets do not show signs of saturation. In the following subsections, we use the term (non-black) saturation to qualify

Table 1
Atomic Data for the Observed Transitions

Ion	$E_{\text{low}}^{\text{a}}$ (cm ⁻¹)	λ_i^{b} (Å)	$g_{\text{low}}^{\text{c}}$	f_i^{d}
H I	0.00	1215.670	2	0.4164
C II	0.00	1334.532	2	0.1290
C II*	63.42	1335.704 ^e	4	0.1277
C IV	0.00	1548.202	2	0.1900
C IV	0.00	1550.774	2	0.0952
N V	0.00	1238.821	2	0.1560
N V	0.00	1242.804	2	0.0780
O VI	0.00	1031.912	2	0.1330
O VI	0.00	1037.613	2	0.0660
Si II	0.00	1190.416	2	0.2770
Si II	0.00	1193.280	2	0.5750
Si II*	287.24	1194.500	4	0.7370
Si II	0.00	1260.422	2	1.2200
Si II*	287.24	1264.730	4	1.0900
Si II	0.00	1304.370	2	0.0928
Si II	0.00	1526.720	2	0.1330
Si III	0.00	1206.500	1	1.6700
Si IV	0.00	1393.760	2	0.5130
Si IV	0.00	1402.770	2	0.2550
S IV	0.00	1062.656	2	0.0500

Notes.

^a Lower-level energy.

^b Wavelength of the transition.

^c Statistical weight.

^d Oscillator strength. We use the oscillator strengths from the National Institute of Standards and Technology (NIST) database, except for S IV, for which we use the value reported in Hibbert et al. (2002).

^e Blend of two transitions; we report the sum of the oscillator strength and the weighted average of λ_i .

absorption troughs of doublets in which $R_a = \tau_i/\tau_j < 0.75 R_l$, where τ_i and τ_j are the AOD of the strongest and the weakest component of the doublet, respectively.

3.2. Column Density Measurements

Computed ionic column densities are determined using the deconvolved line profiles presented in Figure 3 and the ionic transition properties reported in Table 1. The computed column densities are reported in Table 2 for the three absorber models when possible. The adopted values shown in the last column of Table 2 are the ones used in the photoionization analysis. When available, we choose to use the value reported in the PC column as the measurement and use the PL measurement and error as the upper error in order to account for the possible inhomogeneities in the absorbing material distribution. If only the AOD determination is available, we will consider the reported value minus the error as a lower limit unless we have evidence suggesting a high covering.

3.2.1. H I

The spectral coverage of the COS G130M and G160M gratings only allows us to cover the Ly α line that shows a deep and smooth profile in which the different kinematic components blend. The absence of higher-order Lyman series lines restricts us to put a lower limit on the H I column density by applying the AOD method to the Ly α profile.

A better constraint on the H I column density is determined by using higher-order Ly-series lines from earlier *FUSE* data (Dunn et al. 2010). In Figure 4, we compare the 2010 June

Table 2
Computed Column Densities

Trough	v_i (km s ⁻¹)	Ion	AOD ^a (10 ¹² cm ⁻²)	PC ^a (10 ¹² cm ⁻²)	PL ^a (10 ¹² cm ⁻²)	Adopted ^e (10 ¹² cm ⁻²)
T1	-800	H I	73.9 ^{+0.4} _{-0.4}	<900 ^b		∈ [73.5, 900]
		C IV	20.9 ^{+1.1} _{-1.0}	20.9 ^{+1.1} _{-1.0}
		N V	13.9 ^{+1.6} _{-1.6}	18.1 ^{+1.8} _{-1.6}	20.2 ^{+1.6} _{-1.2}	18.1 ^{+3.7} _{-1.6}
		O VI	474 ⁺⁹ ₋₉	745 ⁺¹³⁷ ₋₂₈	...	745 ⁺¹³⁷ ₋₂₈
		Si III	<0.32 ^{+0.04} _{-0.04}	<0.36
T2	-610	H I	436 ⁺⁵⁶ ₋₁	4400 ⁺⁶⁶⁰ ₋₆₆₀	...	∈ [9400, 15800 ^f]
		C II	51.0 ^{+2.4} _{-2.2}	59.7 ^{+3.3} _{-2.9}	...	>48.8
		C II*	43.2 ^{+2.3} _{-2.1}	49.5 ^{+3.2} _{-2.8}	...	≳41.1
		C IV	251 ⁺²⁷ ₋₅	>251
		N V	109 ^{+2.6} _{-2.5}	118 ⁺¹⁵ ₋₂	142 ^{+6.4} _{-3.4}	118 ^{+30.4} ₋₂
		O VI	604 ⁺¹¹ ₋₁₀	816 ⁺¹²⁷ ₋₂₈	1199 ⁺²⁷² ₋₁₁	816 ⁺⁶⁵⁵ ₋₂₈
		Si II	10.5 ^{+0.6} _{-0.6}	13.7 ^{+1.2} _{-0.9}	33.3 ^{+3.5} _{-2.8}	13.7 ^{+23.1} _{-0.9}
		Si II*	1.04 ^{+0.13} _{-0.12}	1.18 ^{+0.18} _{-0.15}	1.59 ^{+0.20} _{-0.17}	1.18 ^{+0.61} _{-0.15}
		Si III	>9.24 ^{+0.16} _{-0.15}	>9.08
		Si IV	36.3 ^{+0.2} _{-0.2}	49.4 ^{+3.7} _{-2.6}	...	>46.8
		Si IV	54.0 ^{+4.5} _{-4.5}	≳49.5
		T3	-440	H I	275 ⁺² ₋₂	4230 ⁺⁷⁹⁰ ₋₇₉₀
C II	19.9 ^{+2.4} _{-2.0}			>17.9
C II*	7.66 ^{+1.55} _{-1.27}			>6.39
C IV	301 ⁺⁵ ₋₅			336 ⁺⁸ ₋₆	432 ⁺⁷³ ₋₈	336 ⁺¹⁶⁹ ₋₆
N V	143 ⁺³ ₋₃			167 ⁺⁷⁸ ₋₅	...	167 ⁺⁷⁸ ₋₅
O VI	552 ⁺¹¹ ₋₉			644 ⁺¹⁷ ₋₁₃	...	644 ⁺¹⁷ ₋₁₃
Si II	<0.66			<0.66
Si III	3.88 ^{+0.09} _{-0.08}			>3.80
Si IV	13.2 ^{+1.1} _{-1.0}			15.9 ^{+1.8} _{-1.0}	17.3 ^{+1.5} _{-1.0}	15.9 ^{+2.9} _{-1.0}
Si IV	<24.2			<24.2
T4	-320	H I	87.0 ^{+0.4} _{-0.4}	550 ⁺¹⁸⁰ ₋₁₈₀	...	550 ⁺¹⁸⁰ ₋₁₈₀
		C IV	62.7 ^{+2.0} _{-1.9}	62.7 ^{+2.0} _{-1.9}
		N V	46.0 ^{+2.2} _{-2.1}	57.5 ^{+4.2} _{-2.8}	67.9 ^{+4.8} _{-3.6}	57.5 ^{+15.2} _{-2.8}
		O VI	335 ⁺⁷ ₋₇	400 ⁺¹⁰ ₋₈	...	400 ⁺¹⁰ ₋₈
T5B	-130	H I	399 ⁺⁵⁰ ₋₁	6010 ⁺¹²⁰⁰ ₋₁₂₀₀	...	6010 ⁺¹²⁰⁰ ₋₁₂₀₀
		C IV	795 ⁺¹⁰⁴ ₋₁₁	>784
		N V	935 ⁺⁸⁰ ₋₁₄	1035 ⁺¹³⁷ ₋₁₄	1469 ⁺²⁸⁴ ₋₇	1035 ⁺⁷¹⁸ ₋₁₄
		O VI	>2608 ₋₂₂	>2586
		Si III	1.78 ^{+0.08} _{-0.08}	>1.70
T5A	-40	Si IV	8.49 ^{+1.13} _{-1.01}	13.7 ^{+11.7} _{-1.9}	...	13.7 ^{+11.7} _{-1.9}
		H I	88.2 ^{+0.5} _{-0.5}	6010 ⁺¹²⁰⁰ ₋₁₂₀₀ ^d	...	∈ [87.7, 7210]
		C IV	97.4 ^{+2.4} _{-2.3}	>95.1
		N V	34.7 ^{+1.8} _{-1.7}	36.7 ^{+1.3} _{-1.3}	40.2 ^{+1.1} _{-1.1}	36.7 ^{+4.6} _{-1.3}
		O VI	>109 ₋₄	>105
		Si III	2.25 ^{+0.06} _{-0.06}	>2.19
Si IV	5.55 ^{+0.72} _{-0.69}	13.7 ^{+176.8} _{-2.6}	...	>13.7		

Notes.

^a The integrated column densities for the three absorber models. The quoted error arises from photon statistics only and is computed using the technique outlined in Gabel et al. (2005a).

^b Estimates from Dunn et al. (2010).

^c Using the covering solution of Si IV (see the text).

^d Dunn et al. (2010) do not make the distinction between the two sub-components in trough T5, so we report an identical PC value in the shallower trough T5A to be considered as a conservative upper limit since the bulk of the column density is coming from T5B.

^e Adopted values for the photoionization study (see the text).

^f The lower is fixed by the detection of Ly10 associated with that component (see the text), and the upper limit is given by the absence of an H I bound-free edge.

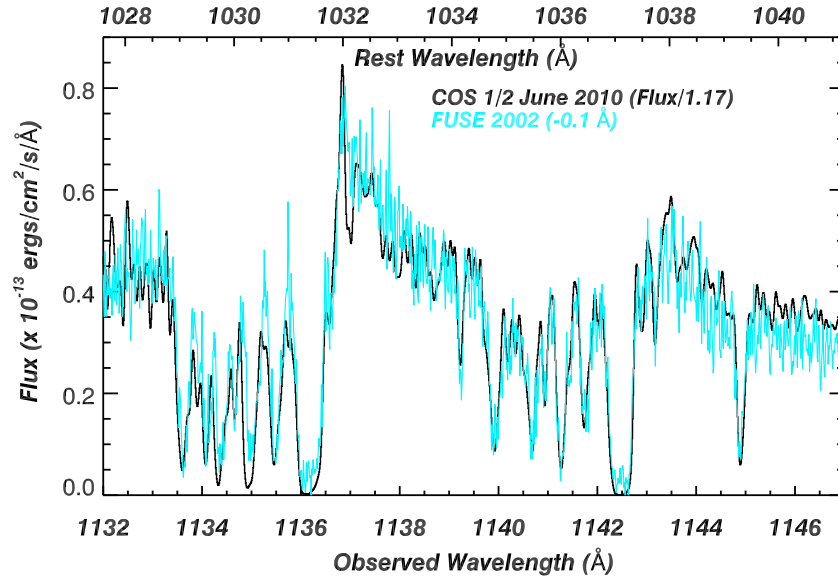


Figure 4. Comparison between the higher-S/N FUSE 2002 and the deconvolved COS 2010 IRAS F22456–5125 spectra in the rest frame O VI region. While the continuum level in 2010 is 17% higher than in the 2002 FUSE observation, the absorption trough profile in the red component does not show significant changes given the limited S/N of the FUSE observation and the larger aperture used by the latter. Changes in the blue line profile seem to be observed in the blue component of the O VI doublet; however, the line profile is located at their edge of the COS detector in a region where the S/N is lower and the wavelength solution is inaccurate.

(A color version of this figure is available in the online journal.)

HST/COS and 2004 *FUSE* spectra of IRAS F22456–5125 in the overlapping region, essentially showing the rest frame O VI region of the spectrum. While we observe a net increase in the continuum flux (a factor of ~ 1.17 between the higher-S/N 2002 *FUSE* observation and the 2010 COS observation) and in the BEL flux between the two epochs, the overall shape of the absorption troughs and continuum remains unchanged. Careful examination of the normalized O VI COS and *FUSE* absorption line profiles reveals troughs that are consistent, given the limited S/N of the FUSE observations, with no variations between the epochs in any of the kinematic components. Therefore, we use the H I column densities determined in the *FUSE* spectrum in our analysis. The H I column density estimates reported in Table 2 are extracted from Dunn et al. (2010) and consist of PC solutions derived on higher-order Ly-series lines. We, however, report the detection of the Ly10 line associated with kinematic component *T2*, revealing an underestimation of the H I column density by a factor of ~ 2 in Dunn et al. (2010). The AOD solutions we report are computed on the Ly α line profile present in the COS spectrum and are only lower limits given the saturation of the line profile. Finally, the absence of a bound-free edge for H I in the *FUSE* data allows us to place an upper limit on the H I column density of $10^{16.2} \text{ cm}^{-2}$.

3.2.2. C IV

Absorption troughs associated with C IV are found in all components of the outflow. The velocity range of the outflow ($\sim 700 \text{ km s}^{-1}$) being greater than the separation between the components of the doublet C IV $\lambda\lambda 1548.200, 1550.770$ ($\sim 500 \text{ km s}^{-1}$) limits the possibility of deriving a PC and a PL solution in several components of the outflow because of self-blending between the red and blue lines of the doublet. While the blue component of trough *T1* is free of known blending, its red component is blended by the blue component of trough *T4*. However, we note that the non-blended part of trough *T4* exhibits the 1:2 strength ratio between the doublet components as expected in the AOD model. Assuming that the covering in trough *T4* is not a strong function of velocity, blending by the

red *T1* line is limited, suggesting that the trough *T1* is also close to AOD. Both red sub-components of trough *T2* are severely blended by the blue components of troughs *T5A* and *T5B*. A lower limit on the column density can be placed on trough *T2* by computing the AOD solution on the non-blended blue line, while a lower limit on components *T5A* and *T5B* is placed by the AOD solution on the non-blended red line. Kinematic component *T3* is the only component where neither C IV of the lines is affected by self-blending, allowing us to determine the ionic column density using all three absorber models.

3.2.3. N V

Absorption troughs associated with N V are observed in every kinematic component of the outflow. Excepting the lower velocity section of trough *T4*, a high covering fraction is indicated by the similarities in the column density computed with the AOD and PC methods. The higher discrepancy observed for component *T1* comes from the fact that the blue N V residual intensity is significantly below the expected level assuming the AOD scenario. Since no blend is known to affect the blue N V, this difference is probably due to a slight overestimation of the emission model in that region, so that the column density determined on the red N V line is probably a reliable measurement of the ionic column density in this component.

3.2.4. O VI

The O VI troughs are located at the edge of the COS detector, where the poor wavelength solution and lower S/N limit the constraints we can put on the ionic column density. While a higher-order correction of the wavelength solution is probably needed at the edge of the detector, we use here a single velocity shift of both the red and blue O VI lines (respectively, 12 and 17 km s^{-1}) in order to align the core of the strongest kinematic components with the centroids of the N V $\lambda 1238.820$ ones. This first-order correction seems to be sufficient for several components; however, the match is not totally convincing for others where a clear shift between the centroid of the blue and red line persists (see Figure 3).

Several components of both red and blue O VI lines are blended by known interstellar medium (ISM) lines, further limiting the accuracy of the column density estimates derived for this ion in several components. The blue O VI line is blended in component *T1* by a weak Fe II $\lambda 1133.880$ and by N I $\lambda\lambda 1134.420$ and 1134.170 in trough *T2* and by N I $\lambda 1134.980$ in trough *T3*. The troughs of stronger ISM lines associated with Fe II and N I at longer wavelengths are shallow, indicating that the blends only marginally affect the line profiles of O VI. In trough *T2*, the red line of O VI is affected by an unidentified blend.

The integrated column densities derived for component *T1* using the AOD and PC model reveal a 60% departure from AOD, suggesting that the PC gives a more realistic estimate of the column. The same behavior is observed in component *T2*. The AOD ratio between the red and blue lines in components *T3* and *T4* is close to the expected laboratory value, suggesting, like in the case of N V, that the AOD determinations can be used. Trough *T5B* is totally saturated in its core and significantly saturated in the wings ($I_r \sim I_b$). The AOD determination in this case is a strict lower limit on the column density since even parts of the red line profile present a residual intensity close to zero ($\tau \gg 1$). The finite ionic column reported in Table 2 for component *T5B* is derived using a maximum optical depth of $\tau = 4$ for these velocity bins. Finally, trough *T5A* shows some evidence for PC effects. However, the presence of an emission hump around 0 km s^{-1} suggests a possible underestimation of the emission model at low velocities around the blue O VI line, decreasing the apparent departure from the AOD scenario for this component. In order to account for this effect, we use the AOD measurement on the red line as a lower limit on the column density in component *T5A*.

3.2.5. Si III

Si III signatures are identified in four of the kinematic components (*T2*, *T3*, *T5A*, and *T5B*) of the UV outflow. A weak feature associated with component *T1* may also be detected in the continuum noise (at less than the 2σ level), though, due to the limits of deconvolution, the deepness of the feature is close to other ripples observed in the continuum and is probably a false detection. Given the nature of the detection, we report an upper limit on the ionic column of Si III for this kinematic component. For the other kinematic components, we are only able to place a lower limit on the Si III column given the impossibility of deconvolving the optical depth from the covering fraction for singlet lines. We note, however, that the Si III trough associated with the kinematic component *T2* shares a residual intensity identical to the one observed Si IV blue (see Figures 3 and 5). Given the non-black saturation noted in Section 3.2.6 in component *T2* for the Si IV line, this observation suggests a net saturation of the Si III trough whose deepness is mainly reflecting a PC effect. We note that the residual intensity of the non-saturated blue N V line is similar to the one observed in the saturated blue Si IV (see Figure 3), which can be a coincidence or point to the fact that the PC model does not constitute an appropriate model of the absorbing material distribution. The residual flux in component *T3* of Si III also shares a similar depth with the blue Si IV line; however, in this case the high covering fraction deduced from the residual fluxes observed in the Si IV doublet lines prevents us from drawing a similar conclusion.

3.2.6. Si IV

Si IV troughs are identified in components *T2*, *T3*, *T5A*, and *T5B*. Trough *T2* shows a significant departure from the AOD

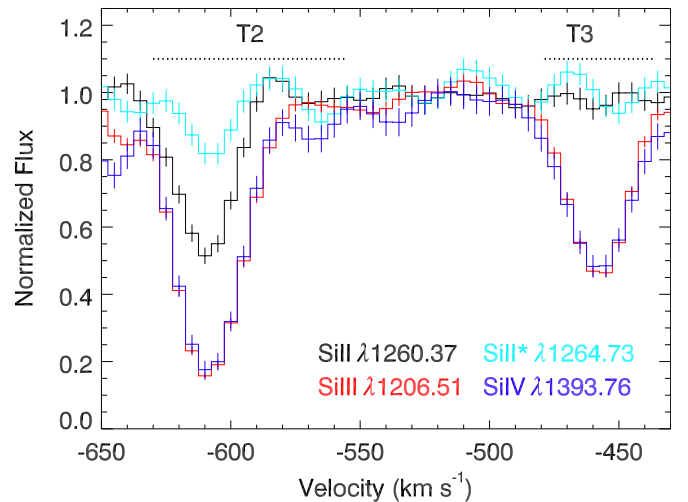


Figure 5. Observation of absorption troughs associated with three different ionization stages of the silicon atom allows us to better constrain the photoionization analysis of the absorber. We also note that the residual intensity in the core of the Si III *T2* troughs matches the saturated blue Si IV, suggesting a non-black saturation of the Si III (see the text). This behavior is also observed in trough *T3*, but leading to a different conclusion due to the non-saturation of Si IV in that case (see the text).

(A color version of this figure is available in the online journal.)

model, suggesting a better description by an inhomogeneous model. Such effect is even stronger in component *T5A*, where the red and blue Si IV line profiles match almost perfectly over the whole component, only allowing us to derive a conservative lower limit on the column by assuming an optical depth limit of $\tau = 4$ in the saturated part of the system. Trough *T3* shows a high covering as revealed by the small difference between the ionic column densities derived by the AOD and PC method. A similar behavior is also observed in trough *T5B* but with a higher discrepancy in the columns due to the difficulty of getting reliable PC measurements for shallow troughs.

3.2.7. Si V

Si V is observed in kinematic component *T2* as a shallow trough. The ionic column density is estimated by applying the AOD method. A shallow feature (less than the 1σ level) in the normalized continuum coincides with the expected position of the Si V line in trough *T3* (see Figure 3), but the feature is similar in depth to other patterns observed in regions free of lines. For this reason we report an upper limit on the Si V line in trough *T3* by fitting the template of the blue Si IV line to the 1σ noise in that region.

3.2.8. The Density Diagnostic Lines

Absorption troughs associated with excited states of Si II and C II are observed in kinematic components *T2* (both Si II and C II) and *T3* (only C II), allowing us to determine the number density and hence the distance to the outflowing material at their origin (see Section 5).

Four absorption troughs from the Si II resonance line ($\lambda\lambda 1190.42, 1193.28, 1260.37, 1526.72$) free of obvious contamination are identified within the COS range associated with the kinematic component *T2* of the outflow. The weaker $\lambda 1304.37$ transition (detected at less than the 2σ level) is located

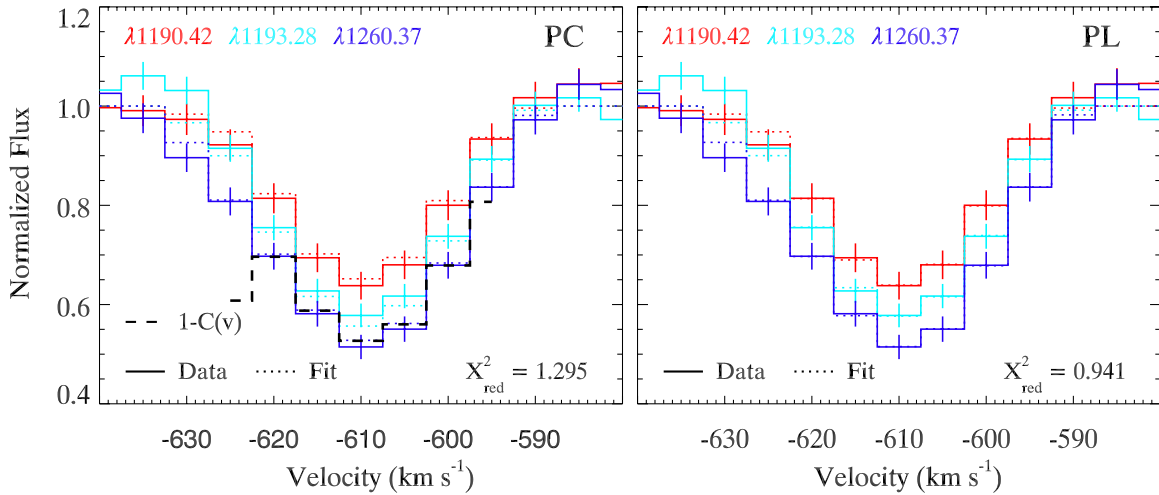


Figure 6. Partial covering (left) and power-law (right) model fit of three Si II resonance lines associated with the kinematic component $T2$ of the UV outflow of IRAS F22456–5125. The original data and their error are plotted in solid while the fitted fluxes are plotted in dotted line. The reduced χ^2 value (see Arav et al. 2008) of the simultaneous fit for the three transitions is given in the bottom right of each panel. The covering solution $C(v)$ is only presented in regions where the residual flux in the weakest lines does not affect the determination.

(A color version of this figure is available in the online journal.)

in a region of lower S/N ⁷ and is barely detected at the S/N level in that region. Observation of four lines emanating from the same state and spanning a range of oscillator strengths allows us to further investigate the absorber model by overconstraining the residual intensity equations. In this case, we have four residual intensities to be fit by two parameters (in the PC and PL models). However, evaluation of the fits to the data by these models requires the knowledge of reliable oscillator strengths of each line.

Despite a number of theoretical studies, large uncertainties remain in the computed oscillator strengths of the Si II transitions (see Bautista et al. 2009 for details). Using the oscillator strengths from NIST for the quoted transitions (rated either B+ or C in the database), we find that the relative strength order of the lines matches the observed residual flux for the $\lambda\lambda 1190.42$, 1193.28, and 1260.37 lines and the weak detection of the $\lambda 1304.37$ transition. This is not the case for the $\lambda 1526.72$ line, which is expected to be weaker than the $\lambda\lambda 1190.42$ and 1193.28 lines (hence having a larger residual flux), but for which we observe a smaller residual intensity across the trough. The problem persists when using the updated oscillator strengths reported in Bautista et al. (2009). While this could be due to a blend, the narrowness of the trough and its location away from any known ISM lines do not support this scenario. For this reason, we use only the $\lambda\lambda 1190.42$, 1193.28, and 1260.37 resonance lines to compute the column density. We present in Figure 6 results of the simultaneous fits of the three Si II lines performed using the PC and PL absorber models. The PC model reveals a small covering factor across the trough, ranging from 0.4 in the wings to 0.5 in the core. A better fit to the observed line profiles is provided using the PL model. The derived PL exponent is close to $a = 10$ across the trough, corresponding to a peaked distribution suggesting that more than half of the emission source is actually covered by optically thin material with $\tau < 0.1$. The results hold if we introduce the weak $\lambda 1304.37$ transition in the computation, leading to

changes in column densities that are less than 10% for both the PC and PL absorber model. The column density derived using the PL absorber model is 2.5 times larger than the one assuming the PC model, potentially suggesting an underestimation of the column density when using the PC model. However, the PL method can overestimate the column density since a good fraction of it originates in the optically thick region ($\tau > 4$) of the distribution, to which the residual flux is not sensitive (see discussion in Arav et al. 2005, 2008). Finally, we note that the integrated column density over $T2$ only differs by less than 7% when one uses the oscillator strength from NIST or the one reported in Bautista et al. (2009).

The strongest transition ($\lambda 1264.73$) associated with the excited Si II ($E = 287 \text{ cm}^{-1}$, Si II* hereafter) is firmly identified in kinematic component $T2$ (see Figure 5). A shallower absorption feature corresponding to the weaker excited transition ($\lambda 1194.50$) is distinguished at the S/N of the COS observations. Detection of two transitions from an ion with the same low energy level allows us, in principle, to derive a velocity-dependent solution of the column density using the PC or PL method. However, the shallowness of the troughs and the limited S/N prevent us from computing a reliable solution across the trough. Nevertheless, we can still derive the column density associated with Si II* assuming a PC or PL model by using the velocity-dependent solution of the covering factor $C(v)$ or the PL parameter $a(v)$ derived above from the fitting of the resonance level transitions of the same ion. With either $C(v)$ or $a(v)$ fixed in the equations of the residual intensity, we constrain the set of two equations of the observed residual intensities in the Si II* lines and are able to derive the velocity-dependent column density solution for both absorber models. In trough $T3$, we put an upper limit on $N(\text{Si II}) < 0.6610^{12} \text{ cm}^{-2}$ due to non-detection (less than the 1σ level) of the stronger $\lambda\lambda 1260.37$ and 1264.73 lines in the COS spectrum.

C II $\lambda 1334.53$ ($E = 0 \text{ cm}^{-1}$) and the blend of C II $\lambda\lambda 1335.66$, 1335.71 ($E = 63 \text{ cm}^{-1}$, hereafter C II*) are detected in components $T2$ and $T3$ of the outflow. Having only one line for each lower level does not allow us to deconvolve the effects of PC and population ratio of the level, allowing us to only provide an AOD estimate. In the case of Si II we saw that the covering

⁷ Given the redshift of the IRAS F22456–5125, the Si II $\lambda 1304.37$ transition is located in a spectral region at the red edge of the G130M grating range and at the blue edge of the G160M grating range.

derived for that ion was quite small, having a covering close to 0.5 in the core of the trough. Looking at the residual intensity in the core of the C II line profile in Figure 7, it is clear that the covering of that line is larger than 0.5. Thus, using the Si II covering solution does not allow us to reproduce the observed C II profiles. In order to tentatively estimate the effect of covering on the C II and C II* columns, we compute the ionic column density using the covering solution derived from Si IV, a medium-ionization species, and report it in Table 2. While we observe a small increase of the derived columns using this PC model, the ratio of column density between the resonance and excited states remains identical (as expected given the similar residual flux inside the C II and C II* troughs), strengthening the density diagnostic obtained from these lines.

4. PHOTOIONIZATION ANALYSIS OF THE ABSORBERS

In order to derive the physical properties of each kinematic component of the outflow, we solve the ionization equilibrium equations using version c08.00 of the spectral synthesis code CLOUDY (last described by Ferland et al. 1998). We model each absorber by a plane-parallel slab of gas of constant hydrogen number density (n_H) and assume solar elemental abundances as given in CLOUDY. The spectral energy distribution (SED) we use was described in Dunn et al. (2010). Using the grid-model approach described in Paper I, we find a combination of total hydrogen column density (N_H) and ionization parameter that best reproduces the observed ionic column densities reported in Table 2. The ionization parameter depends on the distance (R) to the absorber from the central source and is given by

$$U_H = \frac{Q_H}{4\pi R^2 n_H c}, \quad (3)$$

where $Q_H = 2.5 \times 10^{55} \text{ s}^{-1}$ is the rate of hydrogen-ionizing photons emitted by the object and c is the speed of light. We estimate the hydrogen-ionizing rate Q_H (and also the bolometric luminosity L_{Bol}) by matching the flux of the model SED to the de-reddened observed flux at 1150 Å (rest-frame) using a standard cosmology ($H_0 = 73.0 \text{ km s}^{-1} \text{ Mpc}^{-1}$, $\Omega_\Lambda = 0.73$, and $\Omega_m = 0.27$).

The COS observations show a wealth of absorption lines compared to the earlier *FUSE* observations discussed in Dunn et al. (2010). This allows us to derive more accurate physical properties of the absorbing clouds associated with the UV outflow. In the following subsections, we describe the photoionization solution derived for each kinematic component. As discussed in Section 3.2.1, the physical properties of the absorber do not appear to change between the *FUSE* and COS epochs. Therefore, we use the column densities of H I and C III derived in Dunn et al. (2010) from *FUSE* data.

We characterize the maximum likelihood for the model of each kinematic component by the merit function

$$\chi^2 = \sum_i \left(\frac{\log N_{i,\text{mod}} - \log N_{i,\text{obs}}}{\log N_{i,\text{obs}} - \log(N_{i,\text{obs}} \pm \sigma_i)} \right)^2, \quad (4)$$

where, for ion i , $N_{i,\text{obs}}$ and $N_{i,\text{mod}}$ are the observed and modeled column densities, respectively, and σ_i is the error in the measured column density. We prefer this formalism to the traditional definition of χ^2 since it preserves the multiplicative nature of the errors when dealing with logarithmic values.

Table 3
Photoionization Models for Component T2

Ion	$\log(N_{\text{ion}}) \text{ (cm}^{-2}\text{)}$	$\log\left(\frac{N_{\text{mod}}}{N_{\text{obs}}}\right)$	$\log N_{\text{mod}}$		$\log\left(\frac{N_{\text{mod}}}{N_{\text{obs}}}\right)$
			TI _{lo} ^b	TI _{hi} ^b	
$\log U_H$...	-1.9	-2.8	-1.3	
$\log N_H$...	19.1	18.8	18.7	19.1
H I	$\in [15.97, 16.19]$	-0.25	16.38	14.66	+0.20
C II	$\gtrsim 13.95$	-1.16	14.13	10.76	+0.18
C IV	> 14.40	+0.54	14.32	13.96	+0.08
N V	$14.07^{+0.10}_{-0.01}$	+0.40	12.80	14.05	0.00
O VI	$14.91^{+0.25}_{-0.02}$	-0.18	12.18	14.91	0.00
Si II	$13.17^{+0.37}_{-0.03}$	-1.91	13.23	8.45	+0.06
Si III	> 12.96	-0.18	14.01	10.25	+1.05
Si IV	> 13.67	-0.37	13.85	11.14	+0.18
S IV	$\gtrsim 13.69$	+0.11	13.59	12.05	-0.09

Notes.

^a Adopted column densities reported in Table 2.

^b The label SI corresponds to the single-ionization model, while TI_{lo} and TI_{hi} are the low- and high-ionization phases of the two-ionization model of the absorber.

4.1. Troughs T2 and T3

The physical parameters of component T2 are constrained by 10 ionic column densities, eight from COS data along with H I and C III from *FUSE* data (keeping in mind that the latter have been obtained at a different epoch). The ions span a wide range of ionization stages from C II and Si II to N V and O VI. A plot of the results for a grid of photoionization models for trough T2 is presented in Figure 8. The least-squares single-ionization parameter solution ($\chi^2 = 1147$) is marked with a square in the $N_H - U_H$ plane, and predicted values for ionic column densities are given in Table 3. The C II and Si II column densities predicted by that model are underestimating the observed column densities by one and two orders of magnitude, respectively, therefore making the model physically unacceptable. Due to the poor fit of this model to the data, we use a two-ionization component model ($\chi^2 = 6.7$), which is depicted by diamonds in Figure 8. All of the ions from the COS data are fit well with the two-component model (see Table 3).

For component T3, we have column density measurements for seven ions in the COS spectrum, along with H I and C III from *FUSE* data and an upper limit on Si II due to non-detection of the stronger lines in the COS spectrum (see Section 3.2.8). A grid model for trough T3 is plotted in Figure 9. A single-ionization parameter solution ($\chi^2 = 1008$) is marked with a square in the $N_H - U_H$ plane. This solution fits all the lines within a factor of ~ 3 (see Table 4). An improvement to the fit ($\chi^2 = 5.21$) for most ions is provided by the two-ionization parameter solution marked with diamonds in Figure 9, with the exception being an overprediction of Si II by a factor $\gtrsim 4$ (see Table 4).

4.2. Troughs T1, T4, T5A, and T5B

For kinematic component T1, we essentially have five constraints (C IV, N V, O VI, Si III, and H I) defining the region of the (N_H, U_H) parameter space able to reproduce the estimated ionic column densities. Visual inspection of Figure 10 suggests a solution around $\log U_H \sim -0.8$ and $\log N_H \sim 18.6$, consistent with the upper limits on C III from Dunn et al. (2010). This solution ($\chi^2 = 86$) accounts for every constraint to within 0.25 dex. A better solution can be found by relaxing the constraint of solar metallicity. Considering the scaling of elemental abundances

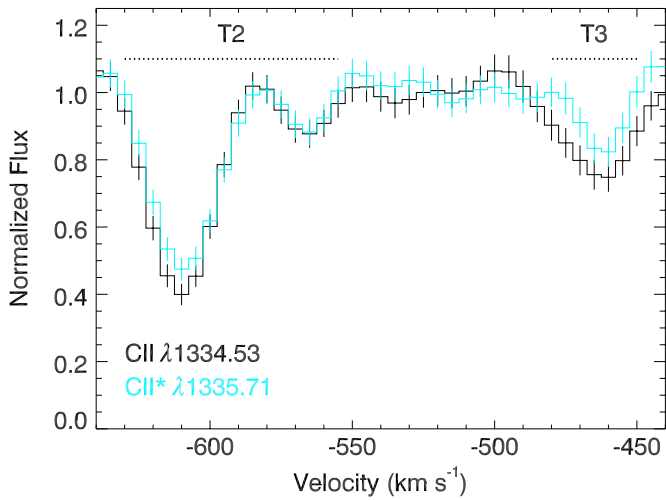


Figure 7. Line profile of C II and C II* rebinned to a common 5 km s^{-1} resolution velocity scale. Absorption troughs are identified in kinematic components T2 and T3 of the outflow.

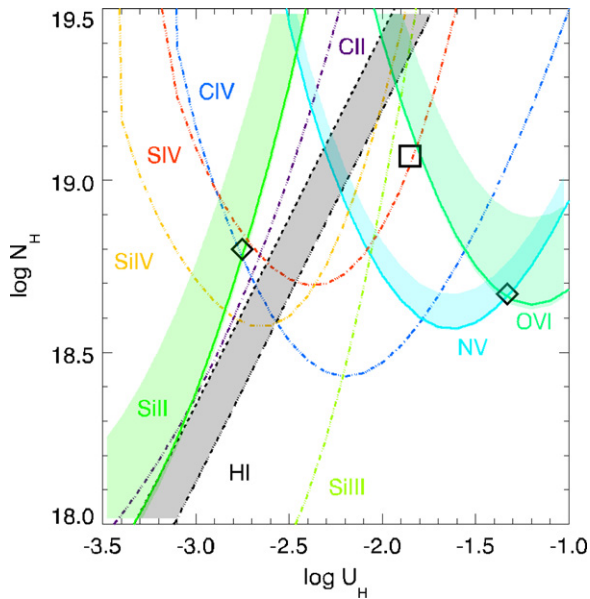


Figure 8. Photoionization modeling of kinematic component T2. The plotted lines represent slab models whose predicted N_{ion} matches the estimated values. Solid lines indicate a measured column density, dotted dashed lines a lower limit on the column density, and dotted lines an upper limit on the column density. The error bars due to the photon noise and the systematic uncertainties in the absorber model are represented as a shaded area for each ion when an estimate is available. The black diamonds mark the two-ionization component model that best fits the estimated N_{ion} , while the black square marks our best single-ionization model.

of C, N, and O as a function of the metallicity Z (Hamann & Ferland 1993; Hamann 1997), an improved solution ($\chi^2 = 0.5$) is found for a gas of sub-solar metallicity ($[Z/Z_{\odot}] \sim -0.4$) using an identical $\log U_{\text{H}}$ and total hydrogen column of $\log N_{\text{H}} \sim 19.1$ for the slab.

The constraints on the $(N_{\text{H}}, U_{\text{H}})$ parameter space for trough T4 are presented in Figure 11. A solution consistent with the measured ionic column densities is found near $\log U_{\text{H}} \simeq -1.4$ and $\log N_{\text{H}} \simeq 18.4$ ($\chi^2 = 2.9$). The solution is suggesting roughly solar abundances of the gas though the slight discrepancy between the measured HI column density and that predicted by the solution may suggest a sub-solar metallicity medium.

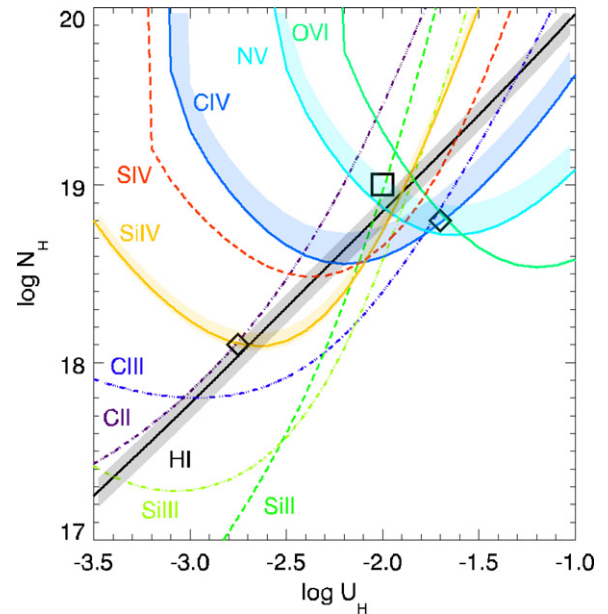


Figure 9. Photoionization solutions to trough T3. Similar presentation as Figure 8.

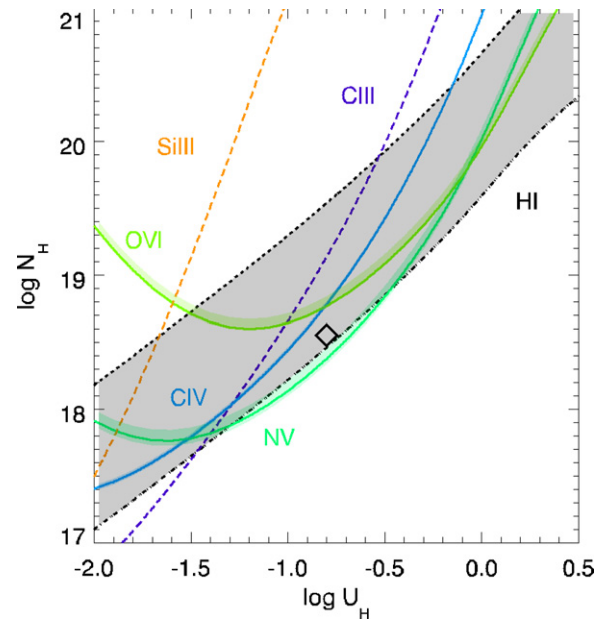


Figure 10. Photoionization modeling of kinematic component T1. Identical description to Figure 8.

The photoionization solution derived for troughs T5B and T5A is presented in Figures 12 and 13, respectively. Inspection of Figure 12 suggests a solution around $\log U_{\text{H}} \sim -1.6$ and $\log N_{\text{H}} \sim 19.5$ ($\chi^2 = 3.6$) for component T5B. A least-squares fit to the constraints available for trough T5A (Figure 13) provides a solution near $\log U_{\text{H}} \simeq -2.0$ and $\log N_{\text{H}} \simeq 18.6$ ($\chi^2 = 27$). While the saturation observed in the troughs of several ions limits the analysis of the physical properties of the gas, the estimated $(N_{\text{H}}, U_{\text{H}})$ solution is able to reproduce most of the ionic columns to within a factor of two.

5. ABSORBER DISTANCE AND ENERGETICS

Detection of resonance and excited state transitions from Si II and C II in troughs T2 and T3 allows us to determine the distance

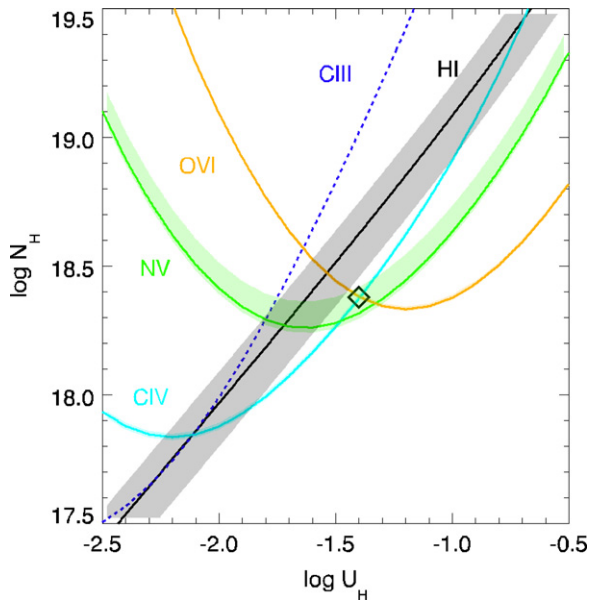


Figure 11. Photoionization modeling of kinematic component *T4*. Identical description to Figure 8.

(A color version of this figure is available in the online journal.)

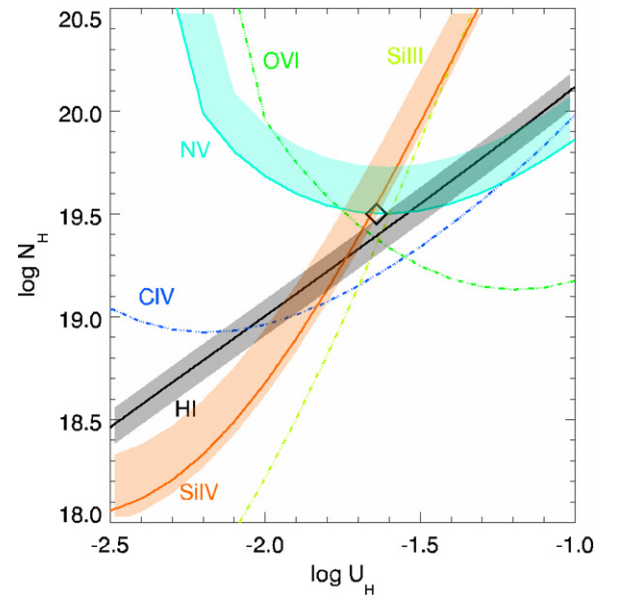


Figure 12. Photoionization modeling of kinematic component *T5B*. Identical description to Figure 8.

(A color version of this figure is available in the online journal.)

Table 4
Photoionization Models for Component *T3*

Ion	$\log(N_{\text{ion}})$ (cm^{-2})	$\log\left(\frac{N_{\text{mod}}}{N_{\text{obs}}}\right)$	$\log N_{\text{mod}}$		$\log\left(\frac{N_{\text{mod}}}{N_{\text{obs}}}\right)$
			$\text{TI}_{\text{lo}}^{\text{b}}$	$\text{TI}_{\text{hi}}^{\text{b}}$	
$\log U_{\text{H}}$...	-2.0	-2.7	-1.7	
$\log N_{\text{H}}$...	19.0	18.2	18.8	18.90
H I	$15.63^{+0.08}_{-0.08}$	+0.10	15.69	15.20	+0.19
C II	> 13.39	-0.45	13.42	11.97	+0.05
C IV	$14.53^{+0.17}_{-0.01}$	+0.36	13.85	14.49	+0.05
N V	$14.22^{+0.27}_{-0.02}$	+0.08	12.44	14.25	+0.04
O VI	$14.81^{+0.01}_{-0.01}$	-0.35	11.93	14.72	-0.09
Si II	< 11.80 ^c	-0.29	12.47	10.23	+0.67
Si III	> 12.58	+0.38	13.36	11.84	+0.79
Si IV	$13.67^{+0.07}_{-0.03}$	+0.21	13.27	12.49	+0.13
S IV	< 13.38	+0.44	13.06	13.18	-0.04

Notes.

^a Adopted column densities reported in Table 2.

^b The label SI corresponds to the single-ionization model, while TI_{lo} and TI_{hi} are the low- and high-ionization phases of the two-ionization model of the absorber.

^c Upper limit set by the non-detection of the stronger Si II and Si II* in that component.

to these two kinematic components from the central source. As can be seen from the definition of the ionization parameter U_{H} (Equation (3)), knowledge of the hydrogen number density n_{H} for a given U_{H} and Q_{H} allows us to derive the distance R . When an excited state is populated by collisional excitation, the population of that state compared to the resonance level depends on the electron number density n_e (Osterbrock & Ferland 2006), which is $\sim 1.2n_{\text{H}}$ in highly ionized plasma. Note that photoexcitation could also populate the metastable levels; however, with an IR flux ~ 0.1 Jy, population of the metastable levels of C II and Si II is negligible in IRAS F22456–5125.

In trough *T2* we observe resonance and excited states from C II and Si II, for which column densities have been derived in Section 3.2.8 and reported in Table 2. In Figure 14, we compare

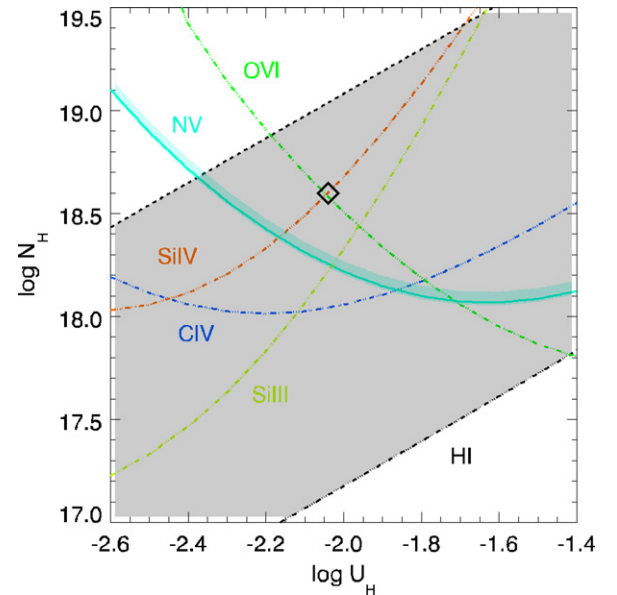


Figure 13. Photoionization modeling of kinematic component *T5A*. Identical description to Figure 8.

(A color version of this figure is available in the online journal.)

computed collisional excitation models for C II and Si II to the measured ratio of the column density between the excited and ground state of these two ions. For the Si II*/Si II ratio, the large uncertainty comes from using PC and PL measurements of the column density associated with Si II* and Si II. The C II*/C II ratio is consistent with the Si II*/Si II ratio. Given the similar but still significantly different residual flux observed in the C II* and C II line profiles, while the value of the column density associated with C II* and C II can change with the different absorber model, their ratio is less affected since both column densities will scale with a similar factor (see Section 3.2.8). For this reason we use the C II*/C II ratio to derive the electron number density of $\log n_e \simeq 1.70^{+0.30}_{-0.15}$ for the low-ionization phase of component *T2*. Using the derived ionization parameter of that

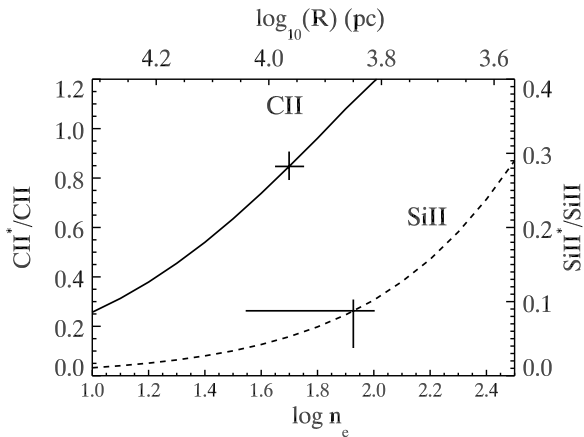


Figure 14. Density diagnostic for kinematic component *T2*. In this figure we plot the theoretical ratio of the level population of the first excited states of C II ($E = 63 \text{ cm}^{-1}$) and of Si II ($E = 287 \text{ cm}^{-1}$) to the level population of the ground state vs. the electron number density n_e for a temperature of 10,000 K (the diagnostic is relatively insensitive to temperature for temperatures typical in UV absorber). The ratios derived from C II and Si II (black crosses) imply an electron number density $\log n_e \simeq 1.7$. The uncertainty on the derived n_e only accounts for the error on the ratio $N_{\text{ion}^*}/N_{\text{ion}}$. On the top axis, we report the corresponding distance as a function of n_e considering the ionization parameter of the low-ionization phase ($\log U_{\text{H}} = -2.8$).

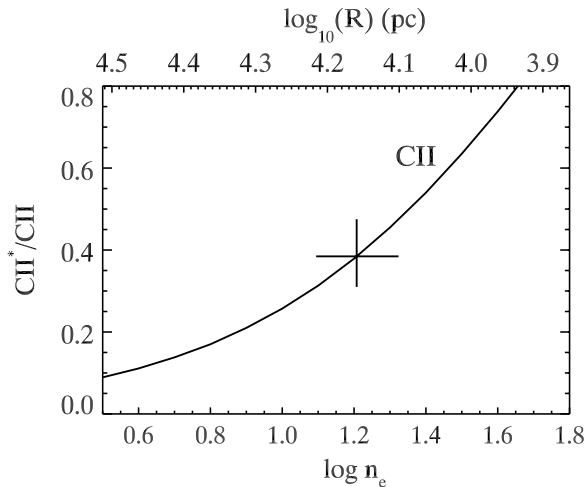


Figure 15. Density diagnostic for kinematic component *T3*. We plot the theoretical ratio of the level population of the first excited states of C II ($E = 63 \text{ cm}^{-1}$) to the level population of the ground state vs. the electron number density n_e for a temperature of 10,000 K. The ratio derived from C II and C II* lines is implying an electron number density $\log n_e \simeq 1.2$. On the top axis, we report the corresponding distance as a function of n_e considering the ionization parameter of the low-ionization phase ($\log U_{\text{H}} = -2.7$).

phase, this density implies a distance of $R \simeq 10.3_{-1.6}^{+5.1}$ kpc, where the errors are conservatively computed from the n_e range allowed by the Si II*/Si II ratio and the error on the ionization parameter. We note that the density derived for this component is consistent with the non-detection of S IV*, only expected to be observed at higher densities.

In trough *T3*, the only excited state we observe is associated with the C II* transitions. Comparing the computed collisional excitation models for C II to the measured ratio of the column density between the excited and ground states of this ion (see Figure 15), we find $\log n_e \simeq 1.20_{-0.10}^{+0.12}$ for the low-ionization gas phase producing the C II and C II* troughs. Given the photoionization solution for that phase quoted in Section 4.1, the derived electron number density implies a distance of

Table 5
Ionization Solution for Each Kinematic Component

Component	$\log(U_{\text{H}})^{\text{a}}$		$\log(N_{\text{H}})^{\text{a}}$ (cm^{-2})	
	This Work	Dunn10 ^b	This Work	Dunn10 ^b
<i>T1</i>	$-0.8_{-0.20}^{+0.24}$	-1.15	$18.6_{-0.21}^{+0.43}$	18.6
<i>T2</i> SI ^c	$-1.9_{-0.15}^{+0.16}$	-1.30	$19.1_{-0.24}^{+0.26}$	19.7
<i>T2</i> TI _{lo} ^d	$-2.8_{-0.05}^{+0.04}$...	$18.8_{-0.04}^{+0.03}$...
<i>T2</i> TI _{hi} ^d	$-1.3_{-0.09}^{+0.10}$...	$18.7_{-0.04}^{+0.07}$...
<i>T3</i> SI ^c	$-2.0_{-0.14}^{+0.15}$	-1.27	$19.0_{-0.18}^{+0.18}$	19.7
<i>T3</i> TI _{lo} ^d	$-2.7_{-0.06}^{+0.08}$...	$18.2_{-0.07}^{+0.07}$...
<i>T3</i> TI _{hi} ^d	$-1.7_{-0.02}^{+0.03}$...	$18.8_{-0.03}^{+0.02}$...
<i>T4</i>	$-1.4_{-0.01}^{+0.01}$	-1.54	$18.4_{-0.01}^{+0.01}$	18.5
<i>T5B</i>	$-1.6_{-0.04}^{+0.04}$	-1.05	$19.5_{-0.01}^{+0.06}$	20.1
<i>T5A</i>	$-2.0_{-0.04}^{+0.04}$...	$18.6_{-0.10}^{+0.09}$...

Notes.

^a The errors we report on our determinations of U_{H} and N_{H} are estimated by size of the contour in the (U_{H} , N_{H}) plane of the solutions that have a χ^2 value twice the χ^2 of the best-fit solution.

^b From Dunn et al. (2010).

^c The label SI corresponds to the single-ionization model.

^d TI_{lo} and TI_{hi} are the low- and high-ionization phases of the two-ionization model of the absorber.

$R \simeq 16.3_{-1.9}^{+3.1}$ kpc, where once again the errors on R reflect the uncertainty in n_e and the ionization parameter. Using the single-ionization solution for component *T3* (see Table 5) leads to a distance estimate reduced by a factor of ~ 2 to $R \simeq 7.3_{-1.3}^{+1.9}$ kpc. Note that in the case of *T3*, we consider the AOD determination of the column densities of C II* and C II given the absence of multiple lines, allowing us to test for the absorber model. Similarly to what is observed for the Si II transitions in kinematic component *T2*, the net difference in residual flux between the excited and resonance troughs could lead an inhomogeneous absorber model to predict a smaller ratio (a factor of two in the case of the Si II*/Si II ratio of trough *T2*). The C II*/C II ratio derived here could then be viewed as an upper limit on the true ratio, the latter being possibly overestimated by up to a factor of ~ 2 , leading to an underestimation of the distance R by a factor of $\sim \sqrt{2}$.

The reported distances are very large compared to the size of the emission regions in AGNs, where we estimate the broad-line emission region to be roughly 0.03 pc in scale (Kaspi et al. 2005). Similar distances to narrow absorption line systems intrinsic to quasars and Seyferts exhibiting lines from excited states of low-ionization species have already been reported in the literature (e.g., Hamann et al. 2001; Hutsemékers et al. 2004; Paper I). The kinematic structure and timescale deduced from the line profiles lend support to the interpretation of these narrow absorption line systems as associated with episodes of mass ejection rather than a continuous wind currently (in the AGN rest frame) emanating from the central regions. In the simplest geometrical picture, we can naively estimate the thickness of each shell of ejected material by $\Delta R = N_{\text{H}}/n_{\text{H}}$, where n_{H} is the hydrogen number density of the low-density, high-ionization phase, giving a $\Delta R < 2$ pc for both components *T2* and *T3*. This is assuming that the individual kinematic components can be described as a uniform slab having internal volume filling factors f of unity. This situation is nonphysical since for the inferred temperature of the absorbing gas ($T \sim 10^4$ K) the velocity width of the outflow ($\Delta v \gtrsim 50 \text{ km s}^{-1}$) is at least 10 times larger than the sound speed, and therefore the outflowing material cannot

Table 6
Physical Properties of the Two Kinematic Components T2 and T3

	$\log U_{\text{H}}$	$\log N_{\text{H}}$ (cm^{-2})	$\log n_e$ (cm^{-3})	R (kpc)	\dot{M}_T ($M_{\odot} \text{ yr}^{-1}$)	$\log \dot{E}_k$ (erg s^{-1})
T2	$-2.8^{+0.04}_{-0.05}$	$18.8^{+0.03}_{-0.04}$	$1.70^{+0.30}_{-0.15}$	$10.3^{+5.1}_{-1.6}$	$5.1^{+2.6}_{-0.9}$	$41.8^{+0.2}_{-0.1}$
	$-1.3^{+0.10}_{-0.09}$	$18.7^{+0.07}_{-0.04}$	$0.20^{+0.31, \text{a}}_{-0.19}$			
T3	$-2.7^{+0.08}_{-0.06}$	$18.2^{+0.07}_{-0.07}$	$1.20^{+0.12}_{-0.10}$	$16.3^{+3.1}_{-1.9}$	$4.1^{+0.9}_{-0.7}$	$41.4^{+0.1}_{-0.1}$
	$-1.7^{+0.03}_{-0.02}$	$18.8^{+0.02}_{-0.03}$	$0.20^{+0.14, \text{a}}_{-0.12}$			

Note. ^a Computed using the low-ionization component number density and assuming that the high-ionization component is located at the same distance from the central source (see Section 6).

be a sonically connected entity. The large Δv of this highly supersonic outflow is then probably due to bulk motion of the absorbing material. Assuming that the outflowing material is not decelerating, we can obtain the dynamical timescale of the shell $t_s = R/v_s \sim 20$ Myr, where we choose an average outflow speed of $v_s = 500 \text{ km s}^{-1}$. Over these 20 Myr taken by the shell to reach the distance R , it has been expanding at a speed $v_{\text{exp}} = \text{FWHM} \sim v/10$ (see Section 2.1), so that $\Delta R \sim 0.1R$. We can use this thickness in order to estimate the actual filling factor f of the shell since $\Delta R = N_{\text{H}}/fn_{\text{H}}$. Using the N_{H} and n_{H} of the high-ionization phase reported for components T2 and T3, we find $f \sim 10^{-3}$. This number is in agreement with the low filling factor ($f_s < 10^{-4} - 0.5$) reported by Blustin & Fabian (2009) based on the comparison of the observed radio flux and predicted flux at 1.4 GHz, though that study was focused on objects possessing an optically thick X-ray absorber.

Therefore, we assume the geometry of the outflowing material to be in the form of a thin ($\Delta R < 1/2R$), partially filled shell, for which we can derive the total mass M_{T_i} in each kinematic component i by

$$M_{T_i} = 4\pi R_i^2 \Omega \mu m_p N_{\text{H}_i}, \quad (5)$$

where $\mu = 1.4$ is the mean atomic mass per proton, m_p is the mass of the proton, Ω is the global covering fraction of the outflow, and N_{H_i} is the total hydrogen column density for the kinematic component. In the case of a two-ionization component model we simply have $N_{\text{H}_i} = N_{\text{H}_{i,\text{lo}}} + N_{\text{H}_{i,\text{hi}}}$. We use $\Omega = 0.5$ since outflows are detected in about 50% of the observed Seyfert galaxies (e.g., Crenshaw et al. 2003). The average mass flow rate \dot{M}_{T_i} is obtained by dividing the total mass of the shell by the dynamical timescale R_i/v_i , and the kinetic luminosity is given by $\dot{E}_{k_i} = 1/2 M_{T_i} v_i^2$:

$$\dot{M}_{T_i} = 4\pi R_i \Omega \mu m_p N_{\text{H}_i} v_i \quad (6)$$

$$\dot{E}_{k_i} = 2\pi R_i \Omega \mu m_p N_{\text{H}_i} v_i^3. \quad (7)$$

The advantage of these formulations is that they use the total hydrogen column density N_{H_i} directly derived from the photoionization modeling of the trough and thus are independent of the filling factor f of the shell or its ΔR . We list the computed values of R , \dot{M}_T , and \dot{E}_k for troughs T2 and T3 in Table 6.

Note that an instantaneous mass flow rate can be defined independently of the dynamical timescale of the outflow by using the physical definition of $\dot{M}_{T_{\text{ins}}} = \rho A v$, where ρ is the mass density of the outflowing material traversing the perpendicular surface A with a velocity v . Using the geometry described above, this formula simplifies to $\dot{M}_{T_{\text{ins}}} = 4\pi R_i^2 \Omega \mu m_p n_{\text{H}_i} f v_i$,

where f is the volume filling factor of the shell. This estimation is directly dependent on the filling factor f of the shell (or its radial extent ΔR), a quantity that is not well constrained observationally. We note, however, that, using the definition of the filling factor ($f = N_{\text{H}}/(n_{\text{H}}\Delta R)$), this instantaneous mass flow rate relates to the average mass flow rate defined in Equation (7) by the relation $\dot{M}_{T_{\text{ins}}} = \dot{M}_{T_i}/(\Delta R/R)$. Since $\Delta R/R \lesssim 0.1$ (cf. Section 5), this means that the average mass flow rates and hence the kinetic luminosities reported in Table 6 are lower limits on the instantaneous mass flow rates.

6. DISCUSSION AND CONCLUSIONS

We analyzed the physical properties of the UV outflow of IRAS F22456–5125 based on high-S/N COS observations. The accurate determination of the column densities associated with the multitude of ionic species detected in the COS FUV range allowed us to derive the physical parameters (U_{H} , N_{H}) of each kinematic component of the outflow. The detection of absorption lines associated with excited states of the low-ionization species C II and Si II in two of the kinematic components allowed us to determine the distance to the absorbing material from the central emission source. In the case of component T2, the density diagnostic derived from the ratio of Si II*/Si II agrees with that derived from C II*/C II, putting the absorbing gas at a distance of ~ 10 kpc. For component T3 only the C II diagnostic line is observed, suggesting a distance of ~ 16 kpc, though that distance could be underestimated by 30% in the case of an inhomogeneous absorber model.

The photoionization solutions we find differ from those found by Dunn et al. (2010) using archival FUSE data (see Table 5). This is due to the limited number of diagnostics available in the FUSE data compared with COS data. The total hydrogen column densities reported in Dunn et al. (2010), derived using only H I and O VI or C III, are generally 0.6 dex higher than the one we find in our analysis. Using the ionization timescale (e.g., Krolik & Kriss 1995) along with the assumption that the column density of H I did not change between two FUSE observations separated by 21 months, Dunn et al. (2010) estimate a lower limit on the distance of ~ 20 kpc to all of the kinematic components of the outflow. The distances we find for components T2 and T3 are roughly consistent with this value. The small discrepancies may be due to the actual light curve over the time period being different from the simple step-function light curve assumed in Dunn et al. (2010).

Despite the large distance and higher velocity of the outflow compared to the one analyzed in Paper I, the reported kinetic luminosities \dot{E}_{k_i} in Table 6 are not energetically significant for AGN feedback. These scenarios generally require kinetic luminosities to be of the order of a few tenths to a few percent of the Eddington luminosity L_{Edd} (e.g., Scannapieco & Oh 2004; Di Matteo et al. 2005; Hopkins & Elvis 2010), while in the case of IRAS F22456–5125, for which $L_{\text{bol}}/L_{\text{Edd}} \sim 0.16$ (Dunn et al. 2008), we find $\dot{E}_{k_i} \sim 10^{-5} L_{\text{Edd}}$. Note that this comparison is probably only a lower limit since it does not take into account the fact that the outflow probably decelerated and lost energy through shocks on the way from the launching region to the actual location R_i . Moreover, studies of UV outflows in Seyfert galaxies typically reveal that an associated warm phase of the outflow, which has an ionization parameter substantially larger than the high-ionization phase we report here (see Table 5) and usually seen in X-rays (Crenshaw et al. 1999), can carry 70%–99% of the kinetic luminosity of the outflow (Gabel et al. 2005b; Arav et al. 2007). Dunn et al. (2010) analyzed that ASCA

and *XMM-Newton* spectra of IRAS F22456–5125 do not reveal any evidence for an X-ray warm absorption edge; however, the limited S/N in these data can still allow the presence of a warm phase with significant column density.

Assuming that the gas is in photoionization equilibrium with the central source, we showed that the large number of constraints available for the determination of the ionization solution of trough *T2* (and in a weaker way in *T3*) reveals that the absorbing material can hardly be described by a slab model characterized by a single U_{H} and N_{H} . Considering a two-ionization solution in which low-ionization species are mainly produced in a phase whose ionization parameter is ~ 1.5 dex smaller than the phase producing the high-ionization N v and O vi, we are able to obtain a better match to the measured ionic column densities for that component (see Table 3). If, as inferred from the kinematic correspondence, the low- and high-ionization components are located at the same distance from the central source, we can derive the density of the high-ionization component to be $n_{\text{H}_{\text{hi}}} = U_{\text{H}_{\text{lo}}}/U_{\text{H}_{\text{hi}}}n_{\text{H}_{\text{lo}}} \sim n_{\text{H}_{\text{lo}}}/30$.

The observation of several absorption lines corresponding to the Si II transition in trough *T2* allowed us to test the absorber model by overconstraining the set of fitted parameters by three residual flux measurements. For that transition we find that the PL absorber model describes the observed residual intensities better than the PC model, similar to what was found by Arav et al. (2008) with the modeling of five Fe II troughs in the spectrum of QSO 2359–1241. Either way, the fits suggest that only a small fraction of the emission source is covered with optically thick material from that low-ionization line. In the same kinematic component we observe a high covering fraction for the high-ionization transition (C IV, N v, O vi), almost consistent to a full covering of the emission source (continuum+BEL+NEL) by those species. Intermediate-ionization species like C II, Si III, or even Si IV show clear signs of intermediate covering. These observations suggest a model where the low-ionization phase is formed by relatively small, discrete clumps of denser material embedded in a lower-density, higher-ionization phase as suggested by Hamann (1998) and Gabel et al. (2005b). We note, however, that the two gas phases are not in pressure equilibrium, questioning the survival of the low-ionization clumps in the more homogeneous high-ionization phase.

Comparing the properties of the outflow present in IRAS F22456–5125 and the bona fide AGN outflow observed in NGC 3783 reveals a more complex situation. Despite their similar kinetic luminosity, the in-depth study of the absorption lines present in the UV spectrum of NGC 3783 revealed the expected signs of an AGN outflow: line profile variability, high velocities ($v \sim 1400 \text{ km s}^{-1}$), high densities ($n_e \sim 10^4$) inferring low distances ($R < 50 \text{ pc}$) to the central source (Gabel et al. 2005b). The large-distance, low-density, low-velocity material found in IRAS F22456–5125 is in comparison also typical of galactic winds (Veilleux et al. 2005). We reported a similar situation in Paper I in the case of the outflowing material present in the quasar IRAS F04250–5718. A key question in that case is to determine whether the galactic wind is driven by the AGN or by starburst activity. While this question has been investigated in the literature, a definite answer is often out of reach for AGNs in which the sustaining conditions for nuclear activity also favor starburst activity (e.g., Veilleux et al. 2005, for a review). While we are not able to determine whether the material is AGN or starburst driven, the PC and the densities

higher than the one typically observed in the intergalactic medium deduced from our analysis suggest that the material is intrinsic to the host galaxy and is hence photoionized by the central source.

We assumed that the ionization structure of the outflow is due to radiation from the central source. We investigated the possibility that the absorber is collisionally ionized by producing grid models of N_{H} versus temperature with a fixed ionization parameter of 10^{-5} . At temperatures $\sim 10^5 \text{ K}$, we reproduce all the metal lines except N v and O vi in trough *T3*. By including another, hotter phase ($T \approx 10^{5.5} \text{ K}$), all of the metal lines are reproduced. However, H I is underpredicted by high-temperature models (a factor of ~ 100 for $\sim 10^{4.8} \text{ K}$ at $\log N_{\text{H}} = 19$). We are therefore led to the conclusion that the ionization structure of the absorber is dominated by photoionization.

B.B. thanks G. Schneider and B. Stobie for providing their IDL implementation of the IRAF RL algorithm and G. Letawe for useful discussions. B.B. also thanks S. Penton for the introduction to the *HST*/COS pipeline. We thank the anonymous referee for a careful reading of the manuscript and suggestions that helped to improve the paper. We acknowledge support from NASA STScI grants GO 11686 and GO 12022, as well as NSF grant AST 0837880.

REFERENCES

- Arav, N., Becker, R. H., Laurent-Muehleisen, S. A., et al. 1999, *ApJ*, 524, 566
 Arav, N., Gabel, J. R., Korista, K. T., et al. 2007, *ApJ*, 658, 829
 Arav, N., Kaastra, J., Kriss, G. A., et al. 2005, *ApJ*, 620, 665
 Arav, N., Moe, M., Costantini, E., et al. 2008, *ApJ*, 681, 954
 Bautista, M. A., Quinet, P., Palmeri, P., et al. 2009, *A&A*, 508, 1527
 Blustin, A. J., & Fabian, A. C. 2009, *MNRAS*, 396, 1732
 Crenshaw, D. M., Kraemer, S. B., Boggess, A., et al. 1999, *ApJ*, 516, 750
 Crenshaw, D. M., Kraemer, S. B., & George, I. M. 2003, *ARA&A*, 41, 117
 Danforth, C. W., Keeney, B. A., Stocke, J. T., Shull, J. M., & Yao, Y. 2010, *ApJ*, 720, 976
 Di Matteo, T., Springel, V., & Hernquist, L. 2005, *Nature*, 433, 604
 Dunn, J. P., Crenshaw, D. M., Kraemer, S. B., & Gabel, J. R. 2007, *AJ*, 134, 1061
 Dunn, J. P., Crenshaw, D. M., Kraemer, S. B., & Trippie, M. L. 2008, *AJ*, 136, 1201
 Dunn, J. P., Crenshaw, D. M., Kraemer, S. B., & Trippie, M. L. 2010, *ApJ*, 713, 900
 Edmonds, D., Borguet, B., Arav, N., et al. 2011, *ApJ*, 739, 7
 Ferland, G. J., Korista, K. T., Verner, D. A., et al. 1998, *PASP*, 110, 761
 Gabel, J. R., Arav, N., Kaastra, J. S., et al. 2005a, *ApJ*, 623, 85
 Gabel, J. R., Kraemer, S. B., Crenshaw, D. M., et al. 2005b, *ApJ*, 631, 741
 Ganguly, R., & Brotherton, M. S. 2008, *ApJ*, 672, 102
 Hamann, F. 1997, *ApJS*, 109, 279
 Hamann, F. 1998, *ApJ*, 500, 798
 Hamann, F., & Ferland, G. 1993, *ApJ*, 418, 11
 Hamann, F. W., Barlow, T. A., Chaffee, F. C., Foltz, C. B., & Weymann, R. J. 2001, *ApJ*, 550, 142
 Hibbert, A., Brage, T., & Fleming, J. 2002, *MNRAS*, 333, 885
 Hopkins, P. F., & Elvis, M. 2010, *MNRAS*, 401, 7
 Hutsemékers, D., Hall, P. B., & Brinkmann, J. 2004, *A&A*, 415, 77
 Kaspi, S., Maoz, D., Netzer, H., et al. 2005, *ApJ*, 629, 61
 Kriss, G. A., Arav, N., Kaastra, J. S., et al. 2011, *Ap&SS*, 335, 257
 Kriss, G. A., Scott, J. E., Alexander, T., et al. 2002, *BAAS*, 35, 146.01
 Krolik, J. H., & Kriss, G. A. 1995, *ApJ*, 447, 512
 Magain, P., Courbin, F., & Sohy, S. 1998, *ApJ*, 494, 472
 Osterbrock, D. E., & Ferland, G. J. (ed.) 2006, *Astrophysics of Gaseous Nebulae and Active Galactic Nuclei*, 2nd ed. (Sausalito, CA: Univ. Science Books)
 Osterman, S., Green, J., Froning, C., et al. 2011, *Ap&SS*, 335, 257
 Scannapieco, E., & Oh, S. P. 2004, *ApJ*, 608, 62
 Schlegel, D. J., Finkbeiner, D. P., & Davis, M. 1998, *ApJ*, 500, 525
 Soifer, B. T., Sanders, D. B., Madore, B. F., et al. 1987, *ApJ*, 320, 238
 Veilleux, S., Cecil, G., & Bland-Hawthorn, J. 2005, *ARA&A*, 43, 769
 Wampler, E. J., Chugai, N. N., & Petitjean, P. 1995, *ApJ*, 443, 586